Chapter 4

The SMART at work

In this chapter standard imaging modes of the SMART are presented. These are summarized in figure 4.1. On the left side, three possible operation modes using photons as excitation source are shown: imaging of the real, reciprocal and energy space. On the right side, the same operation modes are shown but imaging is performed with reflected electrons. One of the many advantages of a spectro-microscope is the possibility to quickly switch between imaging modes. The presentation of the modes will be ordered depending on the settings of the main imaging column. Therefore we will start from the imaging of the real space, followed by the imaging of the back focal plane and the energy dispersive plane. In each section emphasis will be placed on the different information obtainable from the use of photons or electrons.

Since one of the challenges of this work was to implement and use the *first* aberration corrector for low energy microscopes, a subsection (4.1.1) is dedicated to some relevant aspects of the tuning and use of the electrostatic tetrode mirror. Moreover the first proof of aberration correction is shown. Thereafter the latest results in lateral resolution are presented (4.1.2). In the last part of the chapter the imaging of the energy dispersive plane will be presented along with our latest energy resolution results.

4.1 Real space imaging

This is the most often used operation mode. A magnified image of the electrons, emitted or reflected from the sample surface, is transferred to the screen. For high resolution

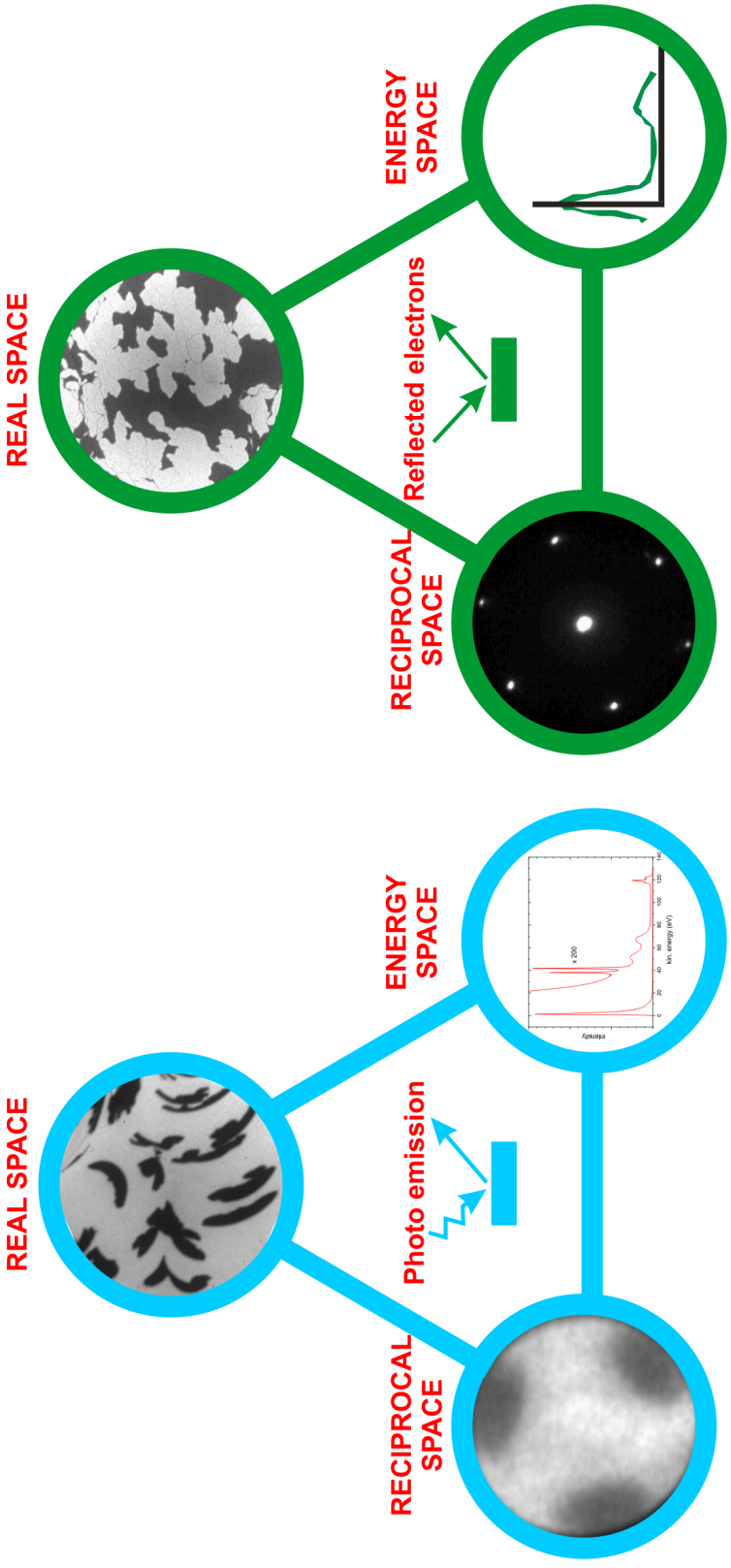

Figure 4.1: Operation modes: Schematic overview of the available operation modes for photoemission (left) and reflection of electrons (right). Adapted from [55].

imaging a normally small contrast aperture and a small exit slit in the analyzer are needed in order to reduce spherical and chromatic aberrations. As a draw back, the improvement in lateral resolution is associated with a decrease in transmission. This was shown by the blue line in figure 2.2 on page 9. The implementation of the aberration corrector not only improves the available lateral resolution by a factor 10, but also the transmission by almost a factor 100. The latter can become a very important issue for, e.g., the investigation of organic surfaces.

Figure 4.2 shows some of the real space operation modes. In images a, b and c the same region is imaged with three different methods. For the first image, the photons emitted from a mercury short arc lamp, with a maximum energy of 4.9 eV, limited by the transmission of the optical elements, have been focused on a small sample region. The energy range of the photons is just in the middle of the typical work function of metals surfaces. The Ag(1 1 1) has a work function slightly lower and therefore appears bright. The kinetic energy range of the electrons is very narrow and depends strongly on the work function. For such cases it is not convenient to use a small aperture in the energy filter. Upon deposition of half a monolayer of organic material the work function is slightly increased and results in a reduction of the photoemitted intensity. This is the main reason for which UV-PEEM is known as being sensitive to changes in the *work function*. Details of the work function changes for the PTCDA thin films on the Ag(1 1 1) and Au(1 1 1) surfaces will be discussed in chapter 5.

Images 4.2.B and 4.2.C have been taken imaging the reflected electrons. The electron beam, collimated in the illumination column and deflected by the magnetic beam splitter, is decelerated in front of the sample from 15 keV to a kinetic energy in the range between 0 and 100 eV. Low energies have to be used in order to minimize the damage to an organic thin film (details on the damage induced by electron beams is found in the work of *U. Groh* [26]). After reflection from the surface the electrons are accelerated to 15 keV again. The interaction of the electrons with the surface can result in elastically and inelastically scattered electrons. The former can produce a characteristic diffraction pattern (in the back focal plane) in an energy range between 1 eV and about 50 eV, while the latter produce diffuse noise (background). The reflection coefficients are usually high (0.1 to 0.5) for the (00) beam in the kinetic energy range below 20 eV. There are two main operation modes in LEEM that are distinguished

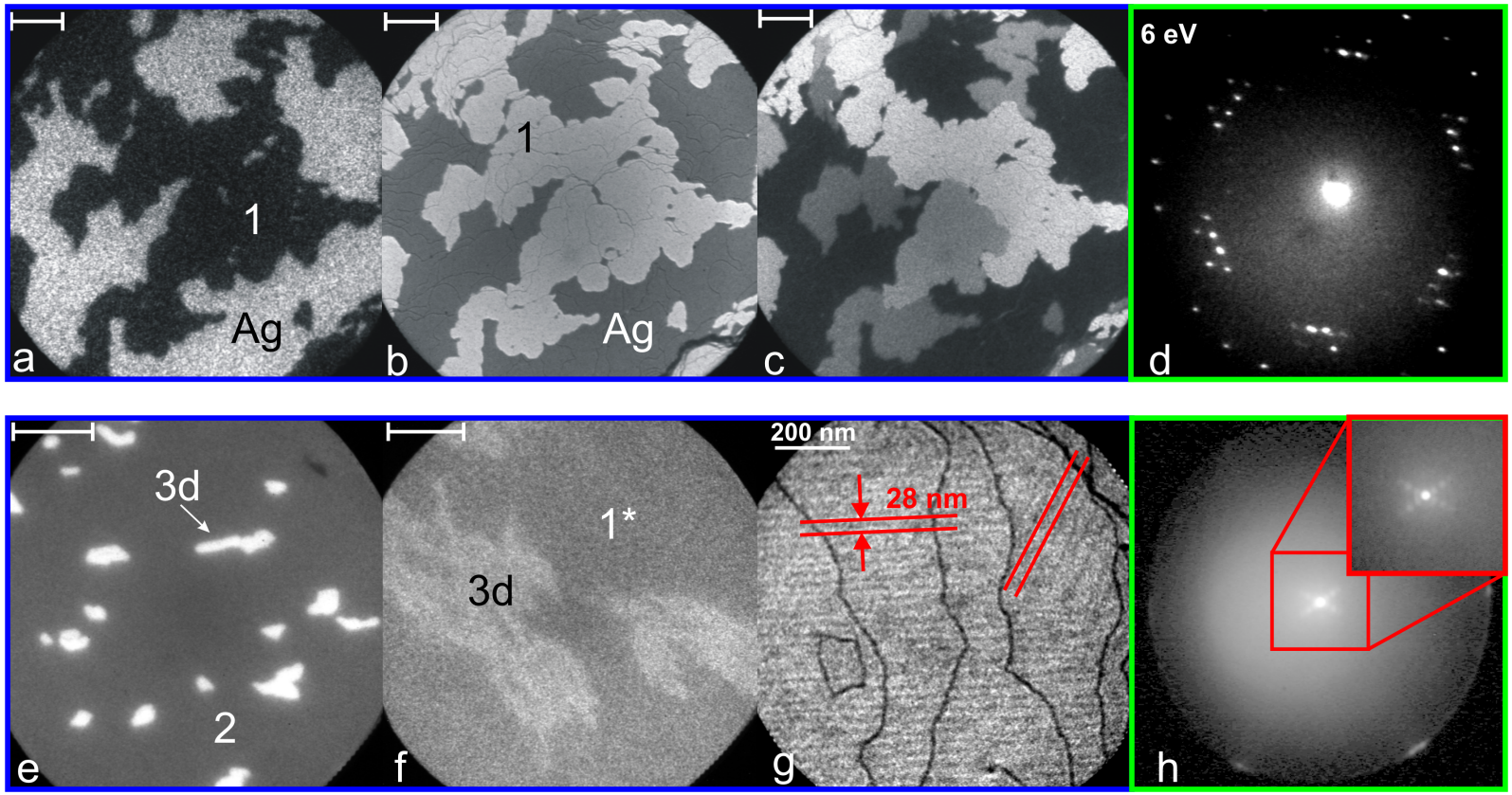

Figure 4.2: Real (blue rectangle) and reciprocal (green rectangle) space operation modes: (a) UV-PEEM, (b) bright field LEEM and (c) dark field LEEM imaging of 0.5 ML PTCDA on the Ag(1 1 1) surface with electron of 2 eV kinetic energy. (d) LEED image of a 5 ML thick PTCDA film on the Ag(1 1 1) surface at 6 eV. (e) NEXAFS-PEEM or laterally resolved NEXAFS imaging of secondary electrons of 5 ML PTCDA/Ag(1 1 1), hν = 285 eV. (f) C1s X-PEEM with hν = 330 eV and 40 eV kinetic energy of 5 ML NTCDA. (g-h) LEEM and LEED images of the Au(1 1 1)—22 $\times$ $\sqrt{3}$ reconstructed surface at 40 eV and 24 eV respectively. Scaling bars are 5 μm (except g and h). The labels Ag, 1, 2 and 3d are for the identification of the Ag substrate and of organic films of different thickness.

according to which diffracted beam is used for imaging: for the *bright field mode* the perpendicularly reflected beam — the (00) beam — is used and for the *dark field mode* one of the diffracted beams — other then the (00) — is used. As a consequence in the former case the intensity, and therefore the signal-to-background ratio, is sufficiently high. For dark field imaging, as the name suggests, the intensity arises *only*[1] from those surface regions that fulfill the periodicity conditions of the selected diffracted beam. Therefore in the obtained image only the selected domains appear bright, while the rest is dark.

The bright field mode is the most commonly used because of the high intensity, which, among other things, facilitates the alignment of the instrument. The transition from bright to dark field mode is done by tilting the incoming beam on the surface so that a desired diffracted beam is then emitted perpendicularly from the surface. Alternatively the aperture in the back focal plane could be displaced, but this would result in higher spherical and chromatic aberrations.

The LEEM imaging is strictly correlated to the diffraction of the electrons at the surface. The electron scattering process resulting in electron diffraction is the reason for which the LEEM method is known to be a *structure-sensitive* imaging technique. Figure 4.2.b shows a bright field image of the same region imaged with UV-PEEM shown in figure 4.2.a. Notice that the contrast inversion is due to two different processes: photoemission and electron scattering. The first is mainly sensible to the work function and the second to the surface structure.

There are many reasons for which LEEM shows a higher lateral resolution. The first of these is the fact that the (00) beam has a low angular divergence which results in low spherical aberrations. The low spherical aberrations are anyhow limiting the lateral resolution. For this reason the next subsection is dedicated to the correction of aberrations in more detail.

4.1.1 Correcting aberrations

The correction of aberrations is only possible by appropriate tuning of the mirror voltages. Theoretical values have been calculated to compensate for all of the possible

[1] Diffuse scattering is not included.

aberration coefficients resulting from the use of our, system-specific, objective lens. The calculation of the voltages in order to obtain a desired set of aberrations has been done using a software written by Dr. Preikszas. We have systematically used the program to obtain the four voltages (three for the mirror and one for the mirror field lens) as a function of spherical and chromatic aberration coefficients. We therefore could fix one of the two spherical or chromatic aberration coefficients and test the effect on the image of the variation of the other aberration coefficient. A schematic plot of the obtained theoretical values is shown in figure 4.3.

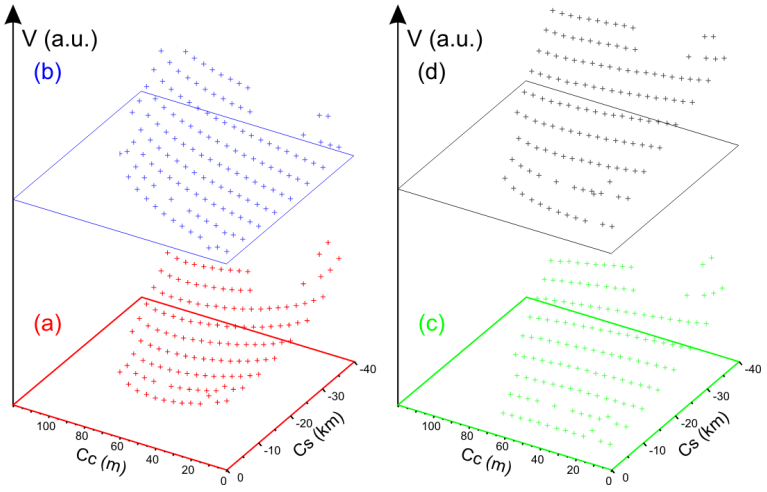

Figure 4.3: Schematic surface plots of the corrector lens potentials. The displayed plots are for the (a) electrode sp0, (b) electrode sp1, (c) electrode sp2 and (d) the mirror field lens.

With these parameters we could then prove that the obtained theoretical values actually worked, i.e. corrected the aberrations. This has been done in the following way. For the spherical aberrations we have imaged a large object and tilted the incoming beam between two incidence angles $\pm\alpha_0$ with respect to the surface normal. We have also made sure that only the reflected (00)-beam was imaged. Since the (00)-beam has a small angular divergence, the resulting imaging of the object can be considered to originate from a *single ray* with an angle α with respect to the surface normal. This *single-ray* is affected by spherical aberration which will cause a displacement of the object in the image plane, with respect to an aberration free image. The displacement is proportional to α^3 (see equation 2.2) as schematically shown in figure 4.4. We fixed the chromatic aberration coefficient of the mirror to 60 m and then

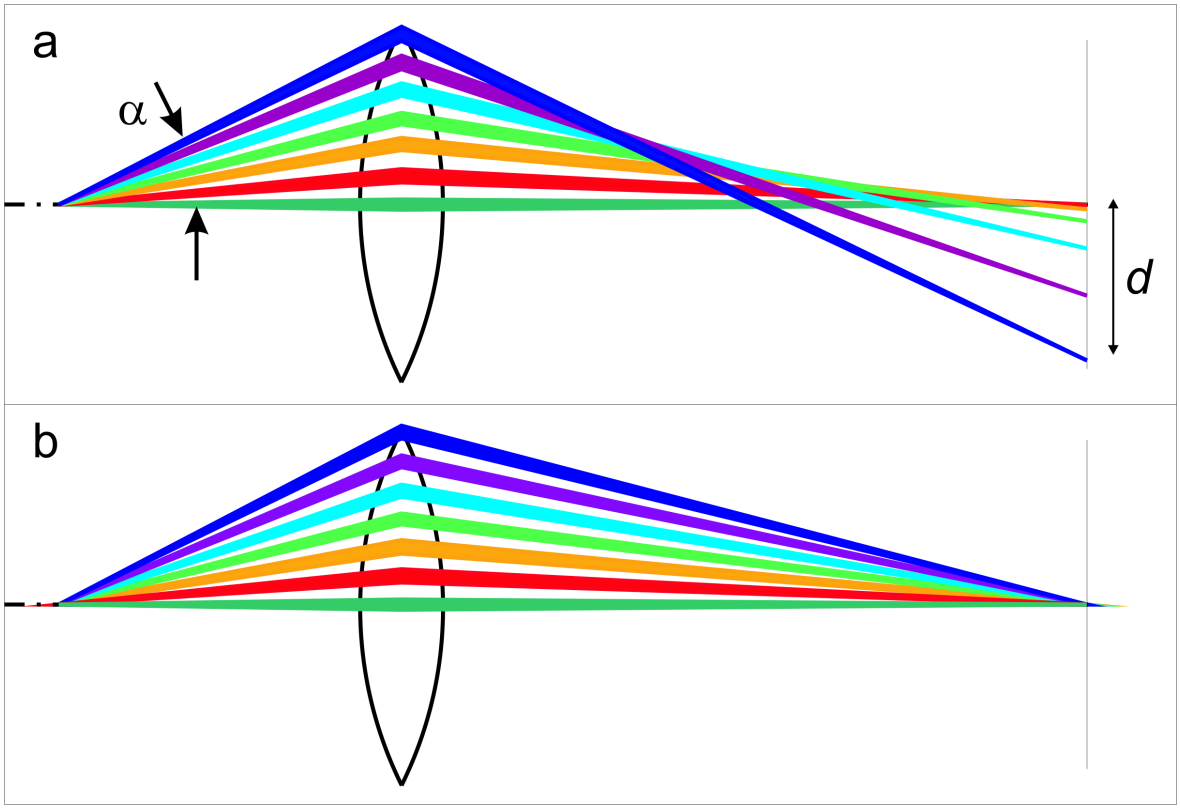

Figure 4.4: Schematic spherical aberration correction: (a) uncorrected system; the displacement d of an object in the image plane, due to spherical aberrations, is proportional to α^3; (b) corrected system.

varied the spherical aberration coefficient. The resulting displacements for an under- and over-compensation of the spherical aberrations are shown in figure 4.5. Upon correct compensation of the spherical aberrations of the objective lens (30 or 40 km, blue and black lines, respectively), the observed displacement of the object is significantly reduced and more importantly does not exhibit a cubic dependance on α.

In a similar way, we have tested the compensation of chromatic aberrations. To do this, we again used LEEM, imaging the reflected (00)-beam, and changed the energy of the incoming electron beam which results in a displacement of the position of the imaging plane for an uncorrected system directly proportional to the energy ($d \propto \Delta E$) as schematically shown in figure 4.6. The position of the imaging plane is measured by adjusting the focus and it is directly proportional to the current of the objective lens.

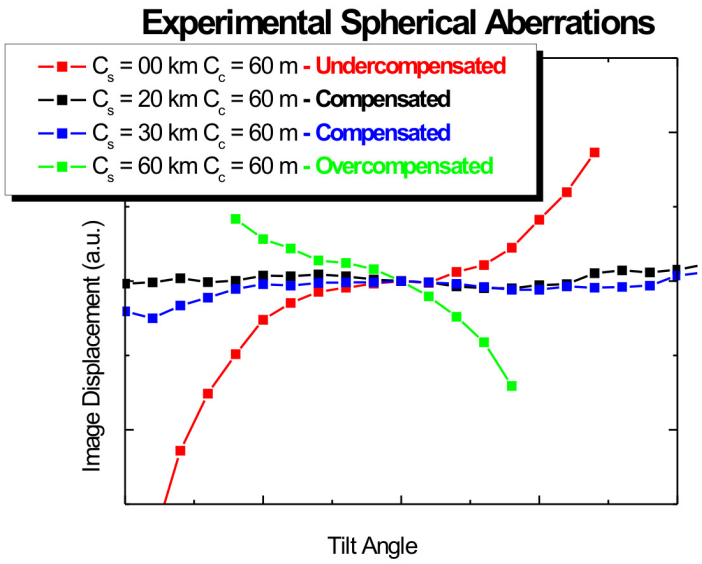

Figure 4.5: Plot of the displacement of an object in the image as a function of α for a set of spherical aberrations compensation values in the mirror with fixed chromatic aberration.

The result is plotted in figure 4.7. We have also slightly varied the spherical aberration coefficient for a better optimization. The best set of values, for (Cc, Cs), were found to be (30m, 20km), (40m, 20km), and (40m, 30km).

This is world wide the first electrostatic mirror used in a PEEM or LEEM and we have successfully proven, for the first time, that it is possible to use the tetrode mirror to compensate for both spherical and chromatic aberrations of the objective lens.

4.1.2 High resolution imaging

The results of the last resolution test are shown in figure 4.8. The first three images on the top (a–c) show the same sample region with three different magnifications. In figure 4.8.d monoatomic steps appear dark due to interference. We assume that the step-width is infinitely small (i.e. a delta function) and convoluted with the instrumental resolution (gaussian). The lateral resolution obtained is of 8 nm and is plotted in the graph in figure 4.8. Since the phase interference contrast at the steps and the presence of impurities adsorbed at steps may cause an additional broadening, the resolution of

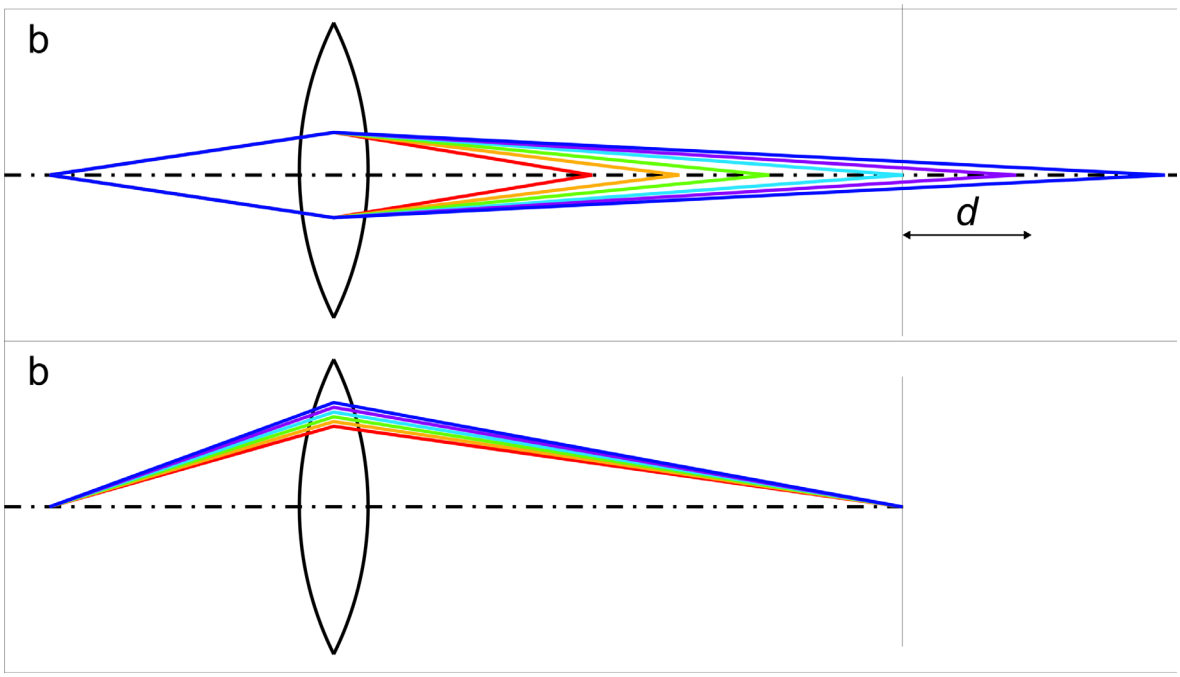

Figure 4.6: Schematic chromatic aberration correction. (a) Uncorrected system. The displacement d of the image plane, due to chromatic aberrations, is proportional to ΔE. The angle α is kept constant. (b) In a corrected system the position of the image plane is fixed.

the instrument is clearly below 8 nm.

4.2 Reciprocal space imaging

To image the Low Energy Electron Diffraction (LEED) or PhotoElectron Diffraction (PED) patterns the back focal plane has to be placed inside the entrance of the energy filter.

We have implemented two reciprocal space imaging modes. In the first mode the back focal plane remains in the contrast aperture (just as in real space imaging). For this reason the contrast aperture has to be removed to view a full spectrum. The surface area producing the pattern is that with low magnification, i.e. small-spot-LEED or -PED can only be obtained by reducing the size of the illumination source. In the second mode the image plane is moved inside the contrast aperture. The area selected for imaging is thus selected with the contrast aperture. This disentangles from the

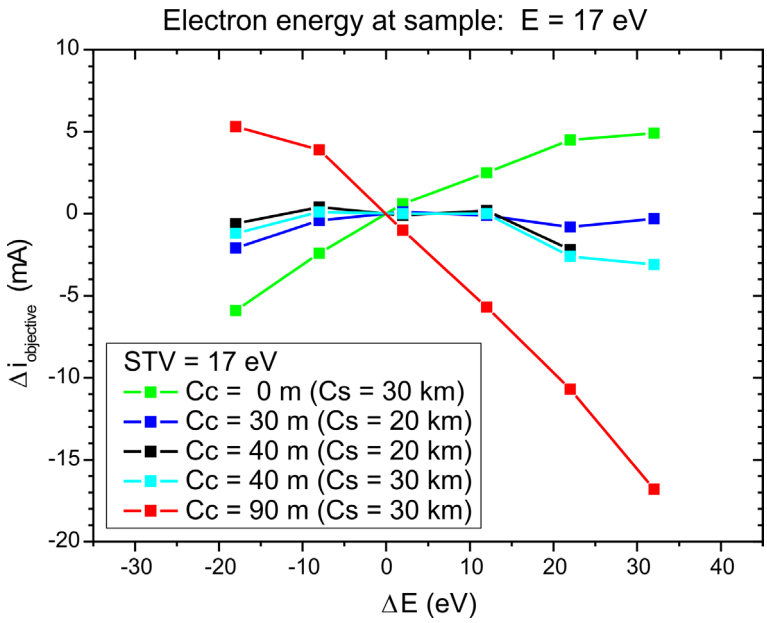

Figure 4.7: Plot of the displacement of the image plane proportional to the current in the objective lens as a function of electron energy, for a set of chromatic and spherical aberration compensation values in the mirror.

problems arising from reducing the size of the illuminated region.

In figure 4.2 frames d and h show two LEED images that have been taken on a Ag(1 1 1) surface covered with 5 ML PTCDA and a clean Au(1 1 1)—22 $\times$ $\sqrt{3}$ reconstructed surface. Compared to a conventional LEED system, the position of the diffraction spots on the screen is fixed for a fixed imaging mode, thus simplifying the acquisition of I(V) curves. Furthermore, it is possible to measure the (00)-diffracted beam intensity at normal incidence. Moreover LEED patterns can be studied at low energies (down to 0 eV).

4.3 High resolution energy space imaging

By adjusting the projection optics, the energy dispersive plane can be imaged. We used this mode to determine the energy resolution of the analyzer. We used a the Ag(1 1 1) substrate and 450 eV photons to excite electrons from the surface. By properly adjusting the sample start voltage, we could image, as shown in figure 4.9, the kinetic

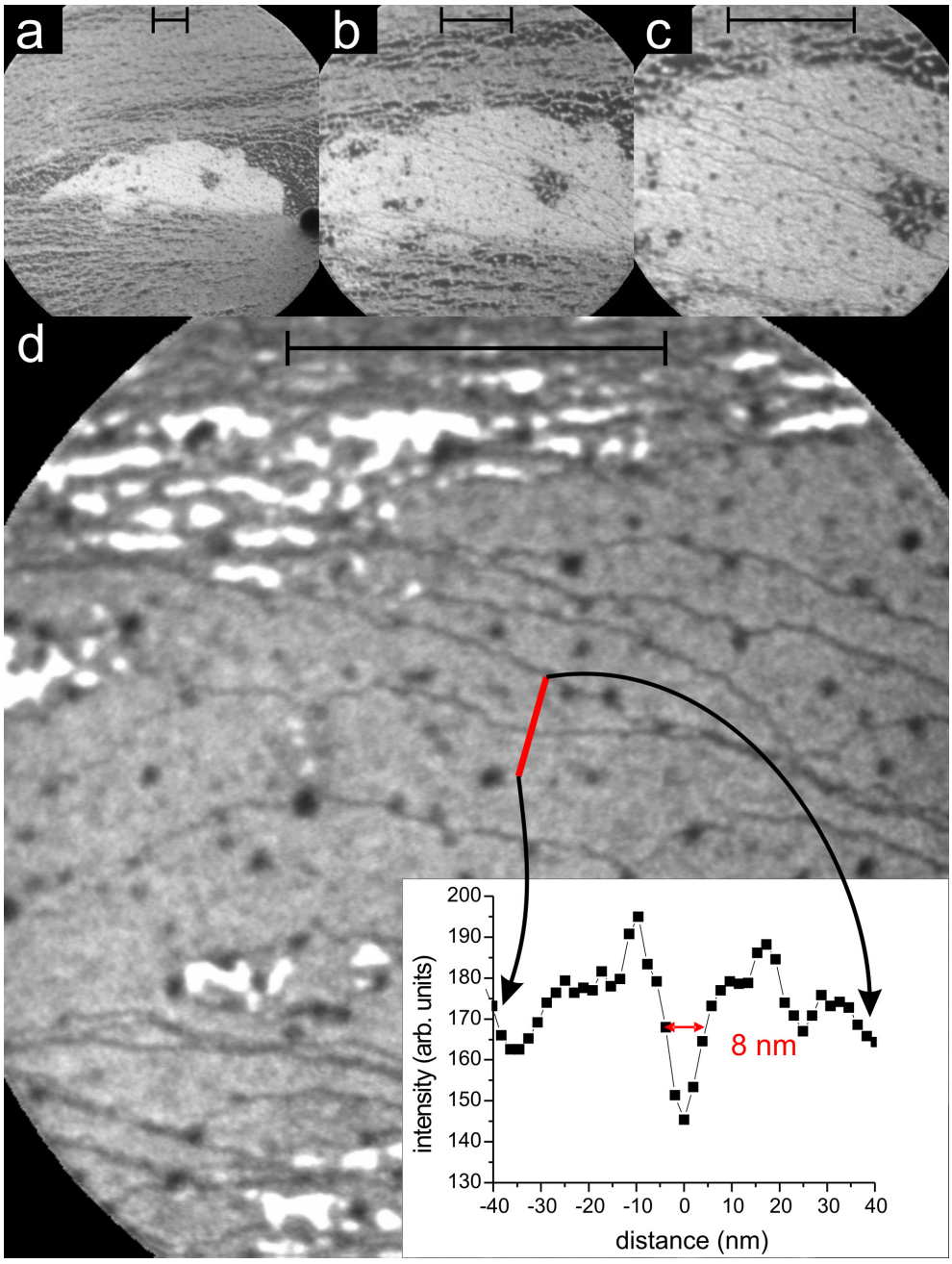

Figure 4.8: Lateral resolution in LEEM. All images have been taken on the Au(1 1 1) surface at kinetic energies of 3.7 eV (A–C) and 18 eV (D). All scaling bars are 400 nm. The plot shows the intensity profile of a single step.

energy region between 70 and 82 eV which icludes the Ag 3d doublet. Using silver is an advantage because the distance between the two peaks, the $3d_{3/2}$ and the $3d_{5/2}$, is fixed to 5.7 eV, with binding energies of 374.0 eV [56] and 368.3 eV [57], respectively. This separation can be used to self-calibrate the energy scale. Furthermore, the lifetime broadening is known to be of 350 meV (Lorentzian) and the fit, with a Voigt function, results in 180 meV of instrumental broadening (Gaussian). By deconvolution of the photon energy resolution of the beam line, which was set to 100 meV, we found an energy resolution at most of 180 meV for the imaging energy filter. This is presently the world record of imaging electron analyzers.

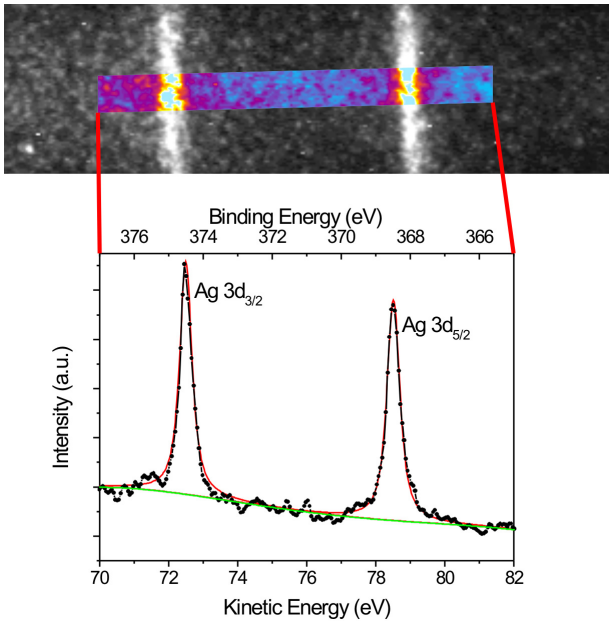

Figure 4.9: XPS spectra of the Ag 3d doublet, taken with the SMART by direct imaging of the dispersive plane. The soft x-ray photon energy is 450 eV. The peaks have a FWHM of 400 meV. The graph shows a fit with a baseline (green) and two Voigt functions (red) yielding a lifetime broadening of the Ag 3d peaks of 350 meV (Lorentzian) and an instrumental broadening of overall 180 meV (Gaussian).